



Cite this: DOI: 10.1039/c5nr07363d

Novel photoswitchable dielectric properties on nanomaterials of electronic core–shell γ -FeO_x@Au@fullerosomes for GHz frequency applications†

Min Wang,^a Chefu Su,^b Tzuyang Yu,^{*b} Loon-Seng Tan,^c Bin Hu,^d Augustine Urbas^c and Long Y. Chiang^{*a}

We unexpectedly observed a large amplification of the dielectric properties associated with the photo-switching effect and the new unusual phenomenon of delayed photoinduced capacitor-like (*i.e.* electric polarization) behavior at the interface on samples of three-layered core–shell (γ -FeO_x@AuNP)@[C₆₀(>DPAF-C₉)]_n **2** nanoparticles (NPs) in frequencies of 0.5–4.0 GHz. The detected relative dielectric constant amplification was initiated upon switching off the light followed by relaxation to give an excellent recyclability. These NPs having e⁻-polarizable fullerosomic structures located at the outer layer were fabricated from highly magnetic core–shell γ -FeO_x@AuNPs. Surface-stabilized **2** in a core–shell structure was found to be capable of photoinducing the surface plasmonic resonance (SPR) effect by white LED light. The accumulated SPR energy was subsequently transferred to the partially bilayered C₆₀(>DPAF-C₉) fullerosomic membrane layer in a near-field (~1.5 nm) region without producing radiation heat. Since the monostatic SAR signal is dielectric property-dependent, we used these measurements to provide evidence of derived reflectivity changes on a surface coated with **2** at 0.5–4.0 GHz upon illumination of LED white light. We found that a high, >99%, efficiency of response amplification in image amplitude can be achieved.

Received 22nd October 2015,
Accepted 13th February 2016

DOI: 10.1039/c5nr07363d

www.rsc.org/nanoscale

Introduction

Molecular organic–inorganic hybrid nanomaterials capable of exhibiting an interactive response in physical (*i.e.* electric and magnetic) properties to electromagnetic waves in the microwave and radio frequency (RF) range remains relatively unexplored to date. Indeed, design of nanoorganic systems to create extraordinary and synergistic material characteristics in the RF range is highly challenging. Artificial structural designs or constructions based on the metamaterial concept show unique electromagnetic properties and a tunable refractive index of the material medium.¹ The basic principles of this phenomenon rest on the ability of the patterned architectures

to interact with the magnetic and electric fields of the incident light waves that result in physical responses leading simultaneously to an unusual electric permittivity (ϵ) and magnetic permeability (μ) not found in nature.^{2–4} However, these artificial designs cannot be extended to the use of organic nanomaterials since they are functionally appropriate only at optical wavelengths.

A tunable multiferroic material requires the use of ferromagnetic materials along with ferroelectrics that are capable of undergoing cross-tuning or switching on the induction of magnetization by means of the electric field or polarization by the magnetic field (magnetodielectric effect).^{5,6} Our related recent study demonstrated the possibility of interactive couplings between dielectric charge electrons (e⁻) of C₆₀(>DPAF-C₉) **1** and magnetic d-spins,⁷ that is, normally, rare in naturally occurring materials. Organic chromophoric systems exhibiting ferroelectric characteristics are limited in availability and remain to be explored.⁸ Early promising organic ferroelectric materials were reported to be two-component co-crystals consisting of phenazine and chloranilic acid.^{9–11} The other example was given by the one-dimensional organic quantum magnet, tetrathiafulvalene-*p*-bromanil charge-transfer complex, *via* polarization.¹² A majority of the

^aDepartment of Chemistry, University of Massachusetts Lowell, Lowell, Massachusetts 01854, USA. E-mail: long_chiang@uml.edu

^bDepartment of Civil and Environmental Engineering, University of Massachusetts Lowell, Lowell, Massachusetts 01854, USA. E-mail: tzuyang_yu@uml.edu

^cFunctional Materials Division, AFRL/RXA, Air Force Research Laboratory, Wright-Patterson Air Force Base, Dayton, Ohio 45433, USA

^dDepartment of Materials Science and Engineering, University of Tennessee, Knoxville, Tennessee 37996, USA

†Electronic supplementary information (ESI) available. See DOI: 10.1039/c5nr07363d

known multiferroic materials, which show simultaneous ferroelectric and ferromagnetic ordering, is the class of binary metal oxides, such as BiFeO_3 ¹³ and BiMnO_3 ferrites. In general, organic multiferroic materials exhibiting both ferromagnetism and ferroelectricity is not readily accessible.

The refractive index value is a function of the product of ϵ and μ , both being relevant material parameters for electromagnetic waves. Interestingly, negative permittivity ($\epsilon < 0$) can be observed on ferroelectric materials.^{14,15} Ferroelectric characteristics arise from the spontaneous polarization and ordering of electric dipoles in response to the external electrical field. Increasingly a common practice to integrate ferroelectric properties and ferromagnetism is to fabricate multiferroic magnetoelectric composite systems, such as ferromagnetic-ferroelectric heterostructures, for the flexibility of creating magnetoelectric effects in the magnetic-field control of electric polarization and also the electric-field control of magnetization.¹⁶ Aside from the magnetic- and electric-field modulation, the use of photoenergy to tune electric polarization and magnetization remains uncommon. One example was demonstrated by the study of photoinduced ferroelectric polarization enhancement on the multilayered thin film structure of a ferroelectric insulator ($\text{Ba}_{0.1}\text{Sr}_{0.9}\text{TiO}_3$) and a ferromagnetic metal ($\text{La}_{0.7}\text{CaSr}_{0.3}\text{MnO}_3$).¹⁷ Photoinduced charge trapping at different sides of the layer interface was attributed to the long-lived screening charges and high polarization. By using these inorganic material systems as guiding models, we designed a highly e^- -polarizable fullerosome membrane with a partial bilayer array of a C_{60} cage sheet located in the center of the membrane to collect negatively polarized charges.

In the case of microwave applications, the tunability of dielectric and magnetic properties with high saturation magnetization and low electrical conductivity based on ferrite-ferroelectric composites would be highly promising for use in tunable microwave devices, such as tunable phase shifters and tunable filters^{18,19} or devices.²⁰ Variation of the composition of the ferrite-ferroelectric composites may also be possible to increase the microwave absorptivity.²¹ Tunable dielectric properties were also proposed to be feasible in polymer composites consisting of short ferromagnetic microwires embedded into a dielectric matrix under a dc magnetic field.²² In the organic system, organic ferroelectric phenomena were observed mainly on crystalline charge-transfer complexes.⁹⁻¹¹ Therefore, we undertook an alternative approach based on the simulation of physical properties of ferroelectricity using C_{60} - and C_{70} -light harvesting chromophore antenna conjugates^{23,24} to demonstrate their photoinduced intramolecular electron-transfer from the donor antenna to the fullerene e^- -accepting cage in an ultrafast kinetic rate in femtoseconds,²⁵ fast enough to simulate "spontaneous polarization" in organic systems. The phenomena produce the intramolecular electron and charge separation of these conjugated C_{60} - and C_{70} -(antenna)_x nanostructures that increases the dielectric characteristics as the real part of the complex dielectric constant (ϵ'_r).

The highly electronegative C_{60} cage is associated with its electron-accepting ability in the presence of a covalently bound

electron-donating chromophore leading to high molecular electron-polarizability characteristics of the conjugate. Intramolecular charge-transfer from the donor moiety to C_{60} can be achieved by the application of an external photoenergy or electrical field that generates a negatively charged $(\text{C}_{60})^-$ cage. The chemical functionalization of C_{60} with organic chromophore groups to produce the corresponding monoadducts and bisadducts, *via* converting one or two fullerene double bonds into two or four, respectively, sp^3 carbons, in general, does not alter much the overall fullerene π -conjugation and photophysical properties.²⁶⁻²⁸ In fact, functional modification of C_{60} disrupts symmetry-forbidden transitions of the parent cage and allows more ground state optical absorption of the derivatives in the visible region.

We have recently reported the synthesis of core-shell paramagnetic nanoparticles (NPs) consisting of highly e^- -polarizable C_{60} (>DPAF- C_9) **1**,²⁹ as a light-harvesting antenna-conjugated [60]fullerene monoadduct.²⁴ Under the design of a core-shell construction, compound **1** exhibited promising molecular polarization responses upon activation by *in situ* photogenerated surface plasmonic resonance (SPR) energy in the preliminary study.²⁹ By way of the multiferroic material approach described above, good tunability of both dielectric (permittivity, ϵ'_r) and magnetic (permeability, μ) properties could lead to a synergic effect on the performance of microwave devices. In addition, based on our recent findings on positive interactive couplings between dielectric electrons of **1** and magnetic d-spins of $\gamma\text{-FeO}_x$ in a bilayered core-shell configuration,⁷ it became an obvious trend to use highly magnetic (superparamagnetic or higher in magnetism) metal oxide particles to enhance such interactions and to tune the permittivity response under a stronger interactive magnetic field. An example of highly magnetic iron oxides was reported³⁰ and produced at high temperatures in the form of monodisperse nanocrystals. These NPs are suitable for this study. Accordingly, we describe here the modified construction of multilayered core-shell NPs with **1**-derived fullerosome arrays deposited as an outer shell layer, based on magnetically enhanced $\gamma\text{-FeO}_x$ cores. They were then used for the study of photoswitchable dielectrics involving interfacial SPR energy transfer events to amplify the dielectric properties of fullerosomes and synthetic aperture RF-signal (SAR) images in the related microwave application at the GHz frequency range.

Experimental

Material preparation

A detailed procedure for the synthesis and spectroscopic characterization of the monoadduct C_{60} (>DPAF- C_9) **1**, 7-(1,2-dihydro-1,2-methanofullerene[60]-61-carbonyl)-9,9-di(3,5,5-trimethylhexyl)-2-diphenylaminofluorene, is provided in the ESI.†

Synthesis of $\gamma\text{-FeO}_x$ ($1.0 < x < 1.5$) nanoparticles. A modified procedure from those reported³⁰ was used. Iron oleate was firstly prepared by heating iron chloride, $\text{FeCl}_3 \cdot 6\text{H}_2\text{O}$ (5.4 g,

20 mmol) and $\text{FeCl}_2 \cdot 4\text{H}_2\text{O}$ (2.0 g, 10 mmol), and sodium oleate (36.5 g, 120 mmol) at 70 °C in a solvent mixture composed of ethanol (80 mL), distilled water (60 mL), and hexane (140 mL), for a period of 4.0 h. At the end of the reaction, the upper organic layer containing the iron oleate complex was washed three times with distilled water (30 mL each), dried over sodium sulfate, and the solvent evaporated off to yield an iron oleate complex in a waxy solid form. To this resulting organometallic complex, 1-oleic acid (4.3 g, 15 mmol) and 1-octadecene (200 g, act as the solvent) were added at room temperature and refluxed at 320 °C for 1.5 h. Upon the temperature reaching 320 °C, a severe exothermic reaction occurred with the initial transparent solution turning turbid and brownish black. The product mixture was cooled to room temperature, followed by precipitation with ethanol (500 mL). The resulting nanoparticles were collected using a permanent magnet, washed twice with both 2-propanol (100 mL) and ethanol (100 mL). They were re-dispersed in a nonpolar solvent, such as hexane and toluene, *via* ultrasonication. In general, the dark solid particles of $\gamma\text{-FeO}_x$ (Fe_3O_4 , ~ 3.5 g) obtained by this method were found to be highly magnetic in response to the external magnet and soluble in many nonpolar organic solvents. The distribution of the particle size is fairly homogeneous and was measured *via* TEM as ~ 20 nm in diameter on average. Spectroscopy data: FT-IR (KBr) ν_{max} 2960 (w), 2921 (s), 2852 (m), 1618 (s), 1459 (w), 1407 (m), and 578 (vs) cm^{-1} .

Synthesis of Au-nanoparticle coated $\gamma\text{-FeO}_x$ nanoparticles, $\gamma\text{-FeO}_x\text{@AuNPs}$. Oleic acid stabilized $\gamma\text{-FeO}_x$ NPs (100 mg) were dissolved in toluene (50 mL) containing 1-oleic acid (1.0 mL). After ultrasonication for 1.0 h and then being dried, it resulted in the deposition or coating of a second layer of oleic acid as an outer layer on the surface of iron oxide NPs. Tetramethylammonium hydroxide (1.0 M, 10 mL, 10 mmol) in D.I. water (100 mL) was added to dissolve the particles and yield a transparent brown aqueous solution. Hydrogen tetrachloroaurate(III) trihydrate ($\text{HAuCl}_4 \cdot 3\text{H}_2\text{O}$, 0.025M, 2.0 mL, 0.05 mmol), sodium citrate dihydrate (14.7 g, 50 mmol), and hydroxylamine hydrochloride (1.0 M, 2.0 mL, 2.0 mmol) were added in sequence under ultrasonication to generate the Au-NP coated $\gamma\text{-FeO}_x$ nanoparticles. The particles was then extracted and stabilized by adding an excess of 1-octanethiol in toluene to give core-shell Au-nanoparticle coated $\gamma\text{-FeO}_x$ nanoparticles (130 mg), $\gamma\text{-FeO}_x\text{@AuNPs}$. Spectroscopy data: FT-IR (KBr) ν_{max} 2958(w), 2921 (m), 2844 (m), 1591 (s), 1398 (s), 1259 (w), 1087 (w), 1016 (w), 966 (w), 904 (w), 808 (m), and 582 (vs) cm^{-1} .

Preparation of C_{60} (>DPAF-C₉)-encapsulated $\gamma\text{-FeO}_x\text{@Au}$ trilayered core-shell nanoparticles, $(\gamma\text{-FeO}_x\text{@AuNPs})\text{@[C}_{60}\text{(}>\text{DPAF-C}_9\text{)]}_n$ **2.** Both $\gamma\text{-FeO}_x\text{@AuNPs}$ (100 mg) and C_{60} (>DPAF-C₉) **1** (100 mg) were dissolved in toluene (30 mL) with stirring for 30 min and then ultrasonicated for an additional >30 min until a clear solution was obtained showing a homogenized nanoparticle dispersion. The solution was concentrated *via* rotary evaporation to less than 3.0 mL in volume to increase the molecular contact of **1** to $\gamma\text{-FeO}_x\text{@AuNPs}$.

It was then diluted by toluene again to a volume of 30 mL with stirring and subsequent sonication for 10 min to dissolve **1** fully. All encapsulated magnetic nanoparticles were physically removed from the container solution with the assistance of an internal permanent magnet. The nanoparticles were washed repeatedly by ethanol and ether, followed by drying *in vacuo* to afford dark brown solids of **2** (187 mg). This method was applied for all subsequent dielectric constants and reflective RF-signal measurements in GHz frequencies. Spectroscopy data: FT-IR (KBr) ν_{max} 2952 (m), 2920 (s), 2848 (m), 1741 (m), 1675 (m), 1637 (m), 1618 (m), 1591 (s), 1490 (m), 1458 (s), 1429 (m), 1382 (m), 1271 (m), 1203 (s), 1168 (m), 1110 (m), 1076 (m), 1029 (m), 875 (w), 811(w), 748 (m), 694 (m), 617 (m), 582 (s), and 526 (s) cm^{-1} .

Dielectric and permittivity measurements

Dielectric property measurements were carried out by an Agilent Network Analyzer equipped with an open-ended Agilent 85070E dielectric probe kit (200 MHz to 50 GHz). Calibration was conducted by using open-ended, close-ended, and attenuated calibrators prior to each measurement to remove the cable-related instability and system drift errors. In the experiment, a complex scattering parameter, defined as S_{11} , was measured and converted to relative complex electric dielectric constant values using Agilent 85071E Materials Measurement Software. This complex form is composed of a real and an imaginary part. The former represents the value of the dielectric constant and the latter is defined as the loss factor.

A LED white light source with the output power of 2.0 W was used in the measurement. Semi-solid poly(dimethylsiloxane) (PDMS, 1.0 g) was used as a polymer matrix host that is capable of forming a paste-like sample with **2**. A mixture of PDMS and either **1**, $\gamma\text{-FeO}_x$ NPs, $\gamma\text{-FeO}_x\text{@AuNPs}$, or NPs of **2** (100 mg) was prepared by dissolving both components in ethyl acetate (20 mL) in a test tube under sonication until a clear solution was obtained. Ethyl acetate was then completely evaporated under vacuum to yield brown paste-like semi-solid materials. A high amount of PDMS was used only in the concentration-dependent permittivity evaluations.

A custom-built chamber was used for dielectric property measurements to be conducted under a circumferentially uniform illumination environment. It was achieved by the installation of a reflective half-circular aluminum plate at the back-wall side surrounding the test tube which is located at the center of the chamber. Light was allowed to pass through a small window at the front side of the chamber to irradiate the test tube containing the sample. Reflected light beams were designed to refocus from the back-side of the aluminum mirror plate back to the tube. Four fans were installed at the top and side-walls of the chamber to control and prevent the temperature build-up inside the chamber. Illumination periods were chosen to be 10, 30, and 60 min.

Reflective RF-signal imaging measurements

In the monostatic synthetic aperture RF-signal (SAR) measurement, only one reflection sensing antenna is needed. A SAR

sensor carrying FMCW (frequency modulated continuous wave) signals was used with a carrier frequency of 10 GHz with a bandwidth of 1.5 GHz and the range distance of 20 cm in all the experiments. The measurement was controlled by an automated biaxial positioner with 8–12 GHz to achieve an accurate spatial registration of the coordinates of the horn antenna. It was performed using a triangular glass plate with or without the sample coating of **2** under illumination for 5.0, 15, or 30 min. Three instants of time were selected to demonstrate the change of reflectivity in the images. The triangular glass plate is a symmetrical triangle with a 30 cm base and a 32 cm height. The coated area is a rectangle (6.8 cm × 5.0 cm) located at 8.0 cm below the apex of the triangle, giving an approximate surface coated area of ~7.0%.

In the rendering of all SAR images, the stripmap SAR mode/algorithm was applied. In these measurements, the glass plate was stationary and placed at 20 cm from the horn antenna in the range direction, while the horn antenna stepped every 1.0 cm for 25 or 36 cm to collect the reflected signals in the cross-range direction. The SAR images of the glass plate with/without the coating were generated from these signals.

The designated core-shell hybrid nanoparticle materials were coated on the triangular glass plate with variable thicknesses for measurement. The sample coating preparation was performed as follows. To a mixture of hybrid nanoparticles (100 mg) and PDMS (1.0 g, variable) was added Sylgard 184 (100 mg, Dow Corning, dielectric constant of 2.6–2.7). It was molded *via* coating on a glass plate which was placed horizontally after polymer curing and dried in a vacuum oven. The cured thin film sample on the plate became non-sticky and immobile. The light source was placed 4.0 inches behind the glass plate to ensure that the entire coated area is covered. The glass plate was illuminated by an LED-white light source. Three instants of time were selected to demonstrate the change of reflectivity in SAR images: (i) before light illumination, (ii) 15 min after light illumination and (iii) the peak response after 30 min of light illumination.

Results and discussion

In our recent studies, we have synthesized and presented an approach for C_{60} /or C_{70} -(antenna)_x type fullerene-chromophore dyads,^{24,25} triads, and pentaads^{31,32} using a C_{60} /or C_{70} (A)-*keto*-DPAF- C_9 (D) assembly structure in femtosecond measurements, where DPAF- C_9 represents 9,9-di(3,5,5-trimethylhexyl)-2-diphenylaminofluorene. This acceptor-donor (A-D) design as that of C_{60} (>DPAF- C_9) **1** (Fig. 1) takes the advantage of both C_{60} > and DPAF- C_9 being active in linear and nonlinear photonic processes.²⁴ Its photoresponsive activity was verified by intramolecular energy/or electron-transfer processes and found to occur in an ultrafast rate of <130 fs.²⁵ In benzonitrile (PhCN), an electron-transfer process was found to dominate the photo-physical events exhibiting the charge-separated (CS) state $C_{60}^{-\bullet}$ (>DPAF⁺- C_n) (Fig. 1) in a long life-time.³¹ A closely linked

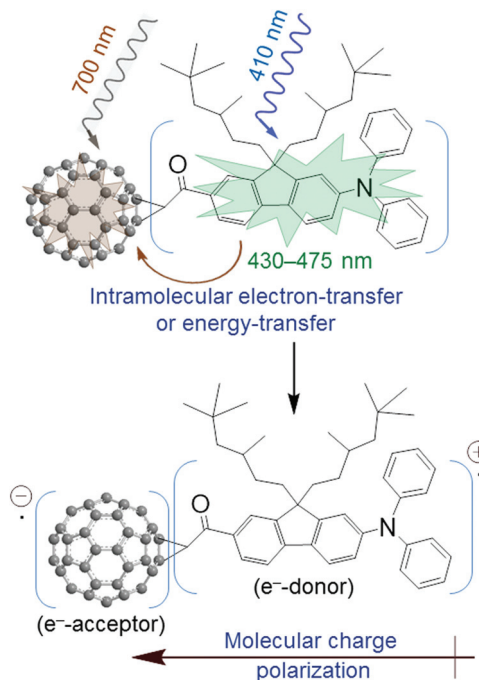


Fig. 1 Conjugation structure of C_{60} (>DPAF- C_9) **1** at the keto conjunction, where the keto-enol isomerization resonance³¹ is omitted, showing optical absorption wavelength ranges of the donor and acceptor moieties and the photoinduced intramolecular e⁻-transfer at a close distance of only a few Å leading to the formation of a molecularly polarized charge-separated state.

molecular nanostructure with periconjugation between C_{60} > and the carbonyl moiety of DPAF- C_n in a spacing distance of only ~3.5 Å (ref. 25) and the concurrence of keto-enol tautomerism at the conjugation bridge²⁹ were the reason for the observed ultrafast photoresponsive rate. The latter leads to the creation of partial conjugation between the e⁻-accepting C_{60} and covalently linked e⁻-donating DPAF- C_n , separated by only one carbon atom (C_{61}) which makes the photoinduced intramolecular electron-transfer very efficient and ultrafast.

The preparation of **1**-encapsulated γ -FeO_x@Au trilayered core-shell nanoparticles, (γ -FeO_x@AuNPs)@[C_{60} (>DPAF- C_9)]_n **2**, as shown in Fig. 2, was carried out first by the synthesis of highly magnetic monodisperse γ -FeO_x nanocrystals using the method modified from the reported procedure³⁰ at 300–320 °C. All other procedures for the layer-by-layer deposition are described in the Experimental section. Synthesis of **1** followed the steps reported.²⁹

Sufficient binding of 1-octanethiol as a capping agent on the surface of γ -FeO_x@AuNPs rendered their moderate solubility in toluene for encapsulation by C_{60} (>DPAF- C_9) **1** under ultrasonication. The resulting relatively pure trilayered core-shell NPs can be retrieved easily from the washing solution (ethanol and ether) by an external permanent magnet. The procedure enabled an efficient separation of core-shell nanoparticles from the residual capping agent and an excess amount of **1** in solution. The binding force of C_{60} (>DPAF- C_9) to the nanoparticle surface was controlled by strong

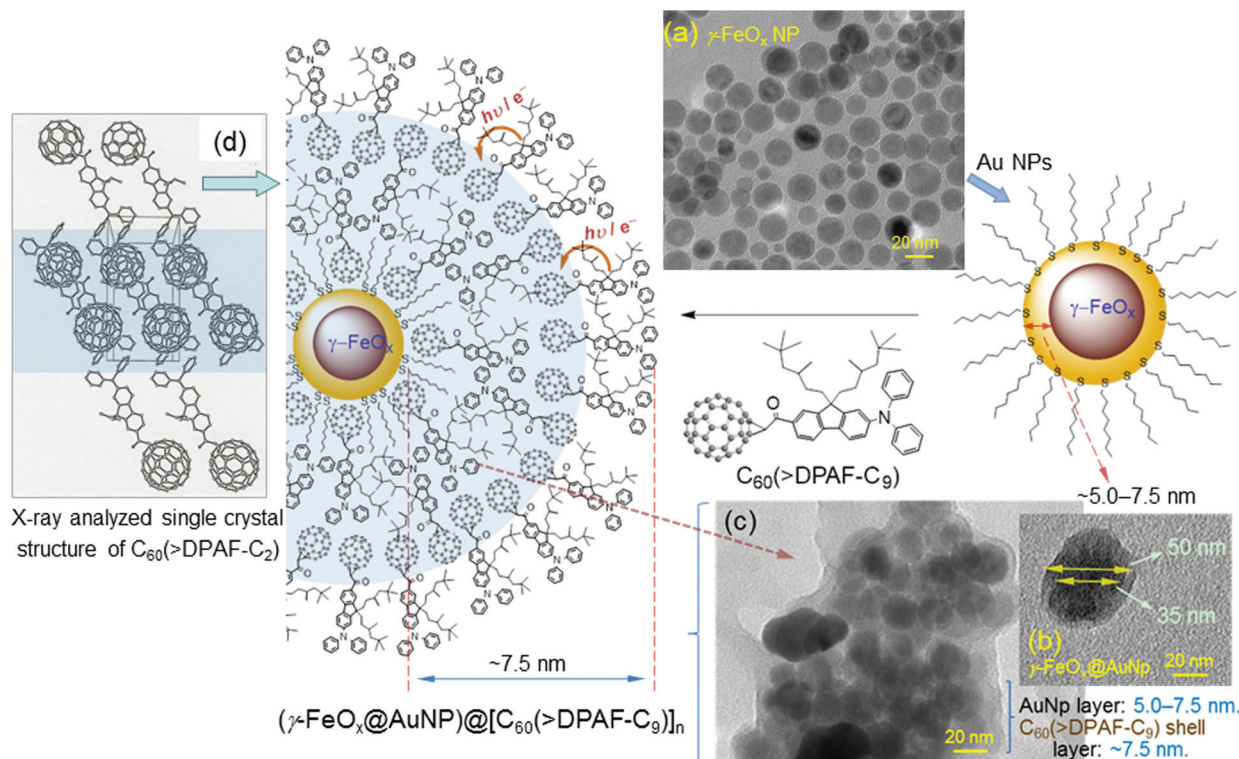


Fig. 2 Synthetic steps for the preparation of 1-encapsulated NPs as trilayered core-shell ($\gamma\text{-FeO}_x\text{@AuNP}@\text{[C}_{60}\text{(>DPAF-C}_9\text{)]}_n$). 2. (a) A TEM micrograph of $\gamma\text{-FeO}_x$ NPs indicating an average particle diameter of 15–35 nm. (b) A representative larger particle of $\gamma\text{-FeO}_x\text{@AuNP}$, by taking 35 nm diameter for $\gamma\text{-FeO}_x$ from (a), the coated Au layer thickness was estimated as indicated. (c) A TEM micrograph of 2 displaying the outer layer of $\text{C}_{60}\text{(>DPAF-C}_9\text{)}$ on NPs with lighter contrast that can be used to estimate a shell thickness as indicated. (d) Schematic presentation of 2 showing a proposed fulleresome array of C_{60} cages, resembling that of $\text{C}_{60}\text{(>DPAF-C}_2\text{)}$ verified by its X-ray single-crystal structural analysis.²⁵

hydrophobic–hydrophobic interaction forces of $(\text{C}_{60}\text{>})\text{-(C}_{60}\text{>})$ cages that resulted in a molecular self-assembly of $\text{C}_{60}\text{(>DPAF-C}_9\text{)}$ molecules to form a partial bilayer or bilayer configuration at the surface, resembling that found on the formation of bilayered fulleresome nanovesicles of water-soluble $\text{C}_{60}\text{(>DPAF-EG}_x\text{)}$ reported recently.³³ Accordingly, the initial interactions of 1 at the nanoparticle surface was designated to occur on two 3,5,5-trimethylhexyl moieties owing to the low solubility of $\text{C}_{60}\text{>}$ in alkanes that should push fullerene cages outward at the solvent interfacial area. The following sonication treatment provides sonochemical energy to invert 1 with the $\text{C}_{60}\text{>}$ cage in contact with the gold nanoparticles³⁴ that gives the monolayer capping of the surface by $\text{C}_{60}\text{(>DPAF-C}_9\text{)}$ molecules. They become accessible for the binding of the second layer of 1 in the solution based on stronger hydrophobic–hydrophobic interaction forces of $(\text{C}_{60}\text{>})\text{-(C}_{60}\text{>)}$ than $(\text{C}_{60}\text{>})\text{-(DPAF-C}_9\text{)}$ aromatic rings. This is proposed as the formation mechanism of a partial bilayered or bilayered fulleresome membrane covering $\gamma\text{-FeO}_x\text{@AuNPs}$ as the nanostructure configuration of 2 shown in Fig. 2.

Morphology and topography investigation of NPs and the core vs. shell thickness of $(\gamma\text{-FeO}_x\text{@AuNP}@\text{[C}_{60}\text{(>DPAF-C}_9\text{)]}_n$ 2 were performed by collecting their transmission electron microscopy (TEM) micrographs (Fig. 2). The average size of the parent $\gamma\text{-FeO}_x$ nanoparticles was measured to be

15–35 nm in diameter in a homogeneous narrow distribution. Upon the deposition of a gold layer in the structure of a $\gamma\text{-FeO}_x\text{@AuNP}$, a slight layer contrast difference was observed to indicate a darker core iron oxide particle diameter of ~ 35 nm with a lighter gold shell thickness of ~ 7.5 nm. Further coating of the $\text{C}_{60}\text{(>DPAF-C}_9\text{)}$ material led to the encapsulation of many nanoparticles by a layer of organic substance in a light soft amorphous image that was measured with a layer thickness of ~ 7.5 nm. This thickness corresponds well with a proposed bilayer packing structure of 1 on the surface of the $\gamma\text{-FeO}_x\text{@AuNPs}$. It is plausible to assume the strong forces of attraction between the $\text{C}_{60}\text{>}$ cage and AuNP in directing the initial orientation of molecules 1 having the fullerene cage directly associated with the surface interfacial binding with the dialkylfluorene ring moiety facing outward to the solution media, as described above. Subsequent packing of more molecules of 1 on the layer of DPAF-C₉ is expectable to form a layer of fulleresome membrane. The estimation of the molecular long-axis length of 1, using the MM2 energy minimization technique to simulate the 3D molecular configuration with the assumption of a C_{60} cage diameter of 1.0 nm, gave a dimension of roughly 3.5 nm. This fits well with the sum of an observed bilayer packing of 7.5 nm in width and an intermolecular physical packing spacing of <1.0 nm.

Energy dispersive spectrum (EDS) measurement, performed on a JEOL JSM 7401F Field-emission Scanning Electron Microscope equipped with an EDAX Genesis XM2 Imaging System, was carried out on a cluster sample of core-shell $\gamma\text{-FeO}_x\text{@Au}$ NPs, as shown in Fig. 3b. In the absence of detectable Au particles in the image, the intensity of the observed Fe and Au peaks in the spectrum (Fig. 3c) can account for an approximate molar ratio of 13 : 1. The spectrum substantiated the coating of a thin Au layer on the $\gamma\text{-FeO}_x$ NPs consistent with the nanoparticle images shown in Fig. 3b.

It is important to note that the optical absorption capability of the Au nanoparticle subshell layer is crucial for this study to allow executing and introducing photoinduced surface plasmon resonance energy generation at visible light wavelengths (400–650 nm). It was followed by the subsequent near-field SPR energy-transfer from the inner layer to the outer $\text{C}_{60}(>\text{DPAF-C}_9)$ -derived fullerosome layer (Fig. 4) upon irradiation of LED white light. The event can be in concurrence with the ability of **1** in **2** to perform a photoinduced intramolecular charge-separation (CS) process themselves to the corresponding transient $\text{C}_{60}^{\cdot-}(>\text{DPAF}^+-\text{C}_9)$ states (Fig. 1) at the similar wavelength range covering roughly 350–430 nm corresponding to the absorptions of DPAF-C₉ moieties. The formation of the CS state can be further enhanced by the SPR-energy. The broad absorption band (Fig. 4b) of the Au layer covering the entire spectrum wavelength range, having the extinction coefficient higher than that of $\gamma\text{-FeO}_x$ (Fig. 4a), should facilitate these near-field SPR photoprocesses efficiently.

Measurements of frequency-dependent complex dielectric properties of **2** were carried out using an open-ended coaxial probe and a network analyzer in the frequency range between 0.5 GHz and 4.5 GHz to study the properties. It includes the real part of relative complex dielectric constant (ϵ'_r) and the

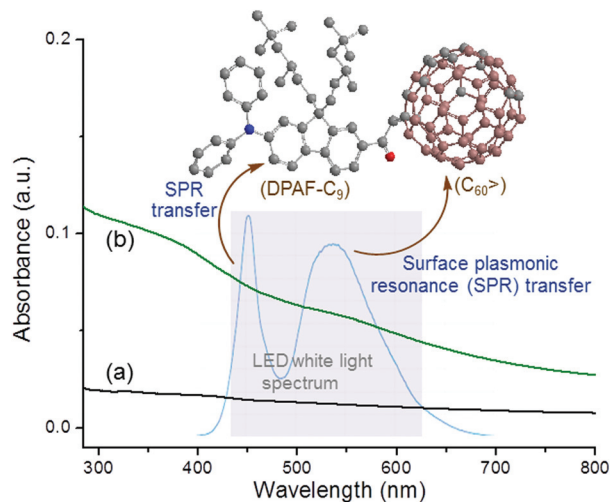


Fig. 4 UV-vis absorption of (a) $\gamma\text{-FeO}_x$ NPs and (b) core-shell $\gamma\text{-FeO}_x\text{@Au}$ NPs with their broad absorption bands overlapping with two emission bands of white LED light used. SPR energy generated from either 450 nm or 540 nm band irradiation is capable of inducing the excitation of DPAF-C₉ or C₆₀> cage moiety, respectively.

relative dielectric loss factor (ϵ''_r , the imaginary part). Measurements were conducted at 10, 30, and 60 min illumination periods. For comparison purposes, five samples were evaluated including $\text{C}_{60}(>\text{DPAF-C}_9)$ alone, $\gamma\text{-FeO}_x$ NPs alone, $\gamma\text{-FeO}_x\text{@}[\text{C}_{60}(>\text{DPAF-C}_9)]_n$ NPs (without a gold layer), $\gamma\text{-FeO}_x\text{@Au}$ NPs, and NPs of **2** in the PDMS mixture. The former two samples were used as references for comparison. The latter three samples allowed us to compare dielectric constants based on nanoparticle shape, size, and magnetic properties. We selected a LED white light source with the output power of 2.0 W for the study. By the use of white light, the optical absorption should occur mainly on the gold layer since the absorption peak maximum (λ_{max}) of the $\text{C}_{60}>$ cage and the DPAF-C₉ moiety is centered at 326 and 410 nm, respectively. A tight packing with minimum air-gap between each particle is critical for the elimination of the influence of air on the ϵ'_r value obtained. In this regard, we used variable quantities of soft poly(dimethylsiloxane) (PDMS) oligomers, with the dielectric constant comparable to that of $\text{C}_{60}(>\text{DPAF-C}_9)$, as a polymer host to fill up any gaps among the nanoparticles after solvent evaporation. We found the ratio of $W_{\text{NP}}/W_{\text{PDMS}}$ equal to 1 : 10 to be an optimal mixture composite to show a good viscosity of the sample and minimum reduction of the ϵ'_r signal as compared with that of the neat **1**.

Fig. 5 shows the relative dielectric constant (ϵ'_r) curves of **1**, $\gamma\text{-FeO}_x$ NPs, and three samples of core-shell nanoparticle materials with the data obtained at 1.0 GHz during and after 60 min illumination using a LED white light source. As a result, no detectable change of ϵ'_r values was observed during or after the irradiation periods with the samples of **1** (Fig. 5B-a), $\gamma\text{-FeO}_x$ NPs (Fig. 5B-b), and core-shell $\gamma\text{-FeO}_x\text{@}[\text{C}_{60}(>\text{DPAF-C}_9)]_n$ NPs (Fig. 5B-c). A noticeable increase of ϵ'_r values was observed

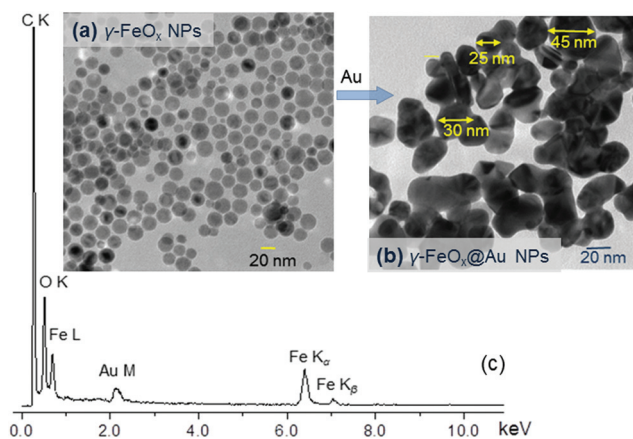


Fig. 3 Micrographic images of (a) $\gamma\text{-FeO}_x$ and (b) $\gamma\text{-FeO}_x\text{@Au}$ NPs, used for the measurement. (c) Energy dispersive spectrum (EDS) of $\gamma\text{-FeO}_x\text{@Au}$ NPs showing the composition where the carbon arises from the carbon tape used for the sample preparation and the oxygen is from both the sample and the environment. The result indicates a molar ratio of Fe : Au as approximately 13 : 1.

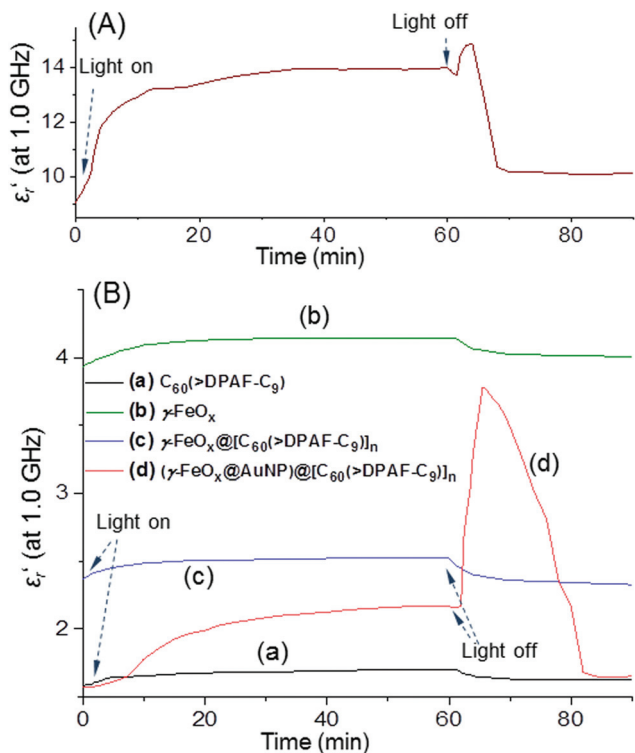


Fig. 5 Large photoswitchable amplification of the relative dielectric constant (ϵ'_r) of trilayered samples of **2** at the light-off state. Time-dependent ϵ'_r profiles of five samples at 1.0 GHz; (A) (γ -FeO_x@AuNP)-PDMS and (B) various samples as indicated.

for the reference sample of γ -FeO_x@AuNPs in the PDMS mixture (Fig. 5A), showing a relatively higher ϵ'_o value of Au (9.0 as compared to 1.56 of **1**) at time zero and 1.0 GHz, during illumination of 2.0–15 min. The ϵ'_r values were then found to be relatively steady in the period of 15–45 min, followed by an increase of permittivity with the ratio of $\epsilon'_{\max}/\epsilon'_o$ in a roughly 1.27-fold with the peak maximum being reached at 8.0 min after the start of light-off state. Since no RF-responses of γ -FeO_x NPs were detected in Fig. 5B-b, changes in Fig. 5A can be correlated to the ϵ'_r value increase of the gold layer owing to the generation of plasmon-energy which was photoinduced by the light applied. Interestingly, on samples of core-shell (γ -FeO_x@AuNP)@[C₆₀(>DPAF-C₉)]_n 2 NPs (Fig. 5B-d), no significant change of ϵ'_r values was shown in the irradiation period from the time zero to 60 min, except the initial Au layer-related permittivity increase at time 10–25 min similar to that of Fig. 5A. Interestingly, the measured relative dielectric constant (permittivity) of **2** only reflects the ϵ'_r value of **1** located at the outer layer with no contribution from the Au layer. It was followed by a large sharp increase of permittivity with the ratio of $\epsilon'_{\max}/\epsilon'_o$ in roughly 2.42-folds at the peak maximum reached at 10-min after the start of light-off state. This is the first observation of a large novel photoswitch-on dielectric constant phenomenon in the GHz-frequency range on organic hybrid nanomaterials. We hypothesized that the long-period storage

of photo-generated plasmonic energy in the intermediate gold layer sandwiched between **1**-derived fullerosome membrane and core γ -FeO_x NPs was effectively released at the light-off state in a near-field of <5.0–8.0 nm (estimate). It causes the activation of the molecular polarization of C₆₀(>DPAF-C₉) molecules, leading to the formation of plasmonic energy-induced transient charge-separate states of **1**, given a positively charged electron-donor moiety of (DPAF)⁺-C₉ and a negatively charged electron-acceptor moiety of the (C₆₀)⁻ cage. These charged transient states are regarded as the origin of the observed high dielectric constant switching-on amplification phenomena. Since the monostatic synthetic aperture RF-signal (SAR) image as a response of reflectivity is dielectric property-dependent, we applied this effect for the purpose of creating tunability and switching capability of reflectivity, as described below.

In similar experiments, we studied the effect of frequency-dependent dielectric and permittivity properties of **2** NPs by evaluation in terms of ϵ'_r and relative loss factors (ϵ''_r) at 0.5–4.5 GHz under illumination with a LED white light source. The inner chamber temperature was monitored constantly during the irradiation period at the sample tube wall. In all experiments, white light illumination led to a slight rise in temperature from 39–52 °C in the first 10 min (Fig. 6a). The increase of chamber temperature resulted in the corresponding small increase of ϵ'_r of the samples in different degrees. There was no clear change of ϵ'_r values (Fig. 6a) of the γ -FeO_x@[C₆₀(>DPAF-C₉)]_n sample without the incorporation of a gold layer at the light switch-off stage, but relaxation returned to the initial ϵ'_r values within 10 min, revealing good recyclability in light-on and light-off cycles.

Significantly different observations were noticed on the samples of **2** prepared by two different methods with the incorporation of a thin AuNP shell layer, as shown in Fig. 6b and c. They displayed the temperature-correlated slight increase of ϵ'_r from 1.56 at time zero to 2.0 during the first irradiation (or light-on) period of 20 min. At the light-off stage immediately after the illumination of 60 min, a large sharp 74% increase of ϵ'_r from 2.163 at the time of 60 min to 3.764 at the time of 68 min (Fig. 6c) at 1.02 GHz within 8.0–10 min after light-off was observed. It was then followed by a relaxation process of ϵ'_r back to a value of 1.56 identical to the initial ϵ'_r indicating a good recyclability of photochemistry involving the AuNP shell and C₆₀(>DPAF-C₉)-derived fullerosome membrane shell.

By the comparison of these data with those of γ -FeO_x@AuNPs, γ -FeO_x@[C₆₀(>DPAF-C₉)]_n, and **1** alone samples, the large difference in the jump of the relative dielectric constant value for **2**-NPs can be correlated to the contribution of the photoinduced generation of plasmonic resonance energy at the AuNP layer with the storage of such energy during the later stage of irradiation followed by the quick energy release at the interface to the outer fullerosome layer immediately after the start of the light-off stage. We believe the phenomena of this type of energy storage is rather novel and realistic since no plasmonic energy converted heat release was detected during the irradiation period of 20–60 min (Fig. 6b and c) in the light

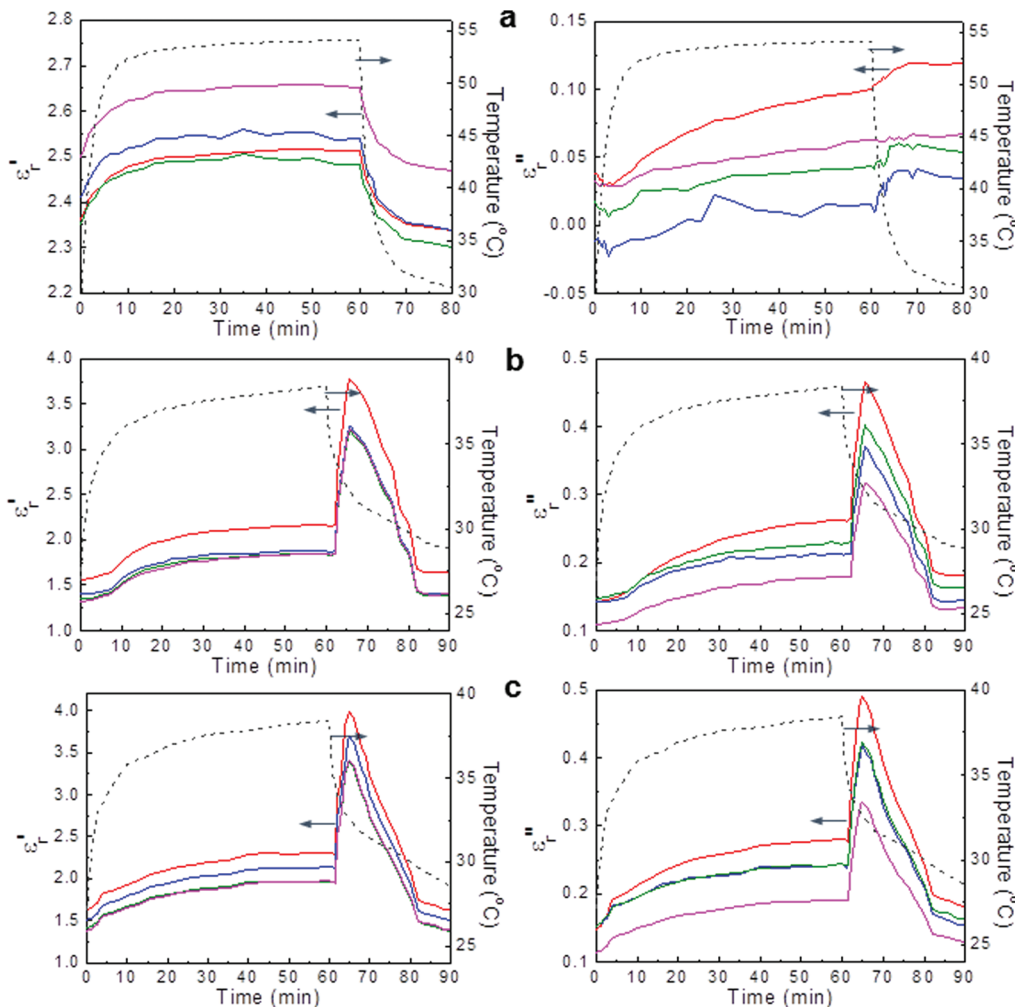


Fig. 6 Dielectric constant curves of samples during and after 60 min illumination by a LED white light. They were measured at frequencies of 1.02 (red), 2.02 (blue), 3.02 (green), and 4.02 (magenta) GHz with the samples of (a) $\gamma\text{-FeO}_x\text{@[C}_{60}(>\text{DPAF-C}_9)]_n$ and (b) and (c) $(\gamma\text{-FeO}_x\text{@AuNP})\text{@[C}_{60}(>\text{DPAF-C}_9)]_n$. Samples of (b) and (c) were synthesized by slightly different methods. The dash line of $^\circ\text{C}$ values is shown on the right y-axis.

of a relatively steady ϵ'_r value throughout this time period. We propose that the release of interfacial plasmonic resonance energy was absorbed by fullerenes leading to the activation or induction of molecular polarization within the $\text{C}_{60}(>\text{DPAF-C}_9)_x$ conjugate.

In fact, we have previously demonstrated the phenomena of efficient photoinduced intramolecular charge separation of **1** in polar media using nanosecond transient spectroscopy measurements.³⁵ Photoexcitation of **1** resulted in the formation of a transient CS state of these nanomaterials with a configuration consisting of a positively charged $(\text{DPAF-C}_9)^+$ and a negatively charged $(\text{C}_{60})^-$. With the increase of the number of DPAF- C_9 antenna moieties attached to the same C_{60} cage from 1 to 4, the lifetime (τ_{CS}) of these charge-separated transient states was found to be prolonged to >900 ns,³¹ sufficiently long enough for contribution to dielectric properties. Accordingly, we regarded the *in situ* generation of these CS states within the outer shell layer of **2** NPs as the

source of electric charges to amplify the observed permittivity in the RF range. The characteristics of the high recyclability of this type of core-shell nanoparticles during the light-on and light-off manipulation may allow their use as permittivity (dielectric)-switching nanomaterials in tunable RF devices. A further tunability and switching capability study of distant monostatic images and angle-dependent reflective RF-signals should give certain insight into our study of RF signal-tunable coating applications.

The value of dielectric constant was detected to be decreasing with the increase of RF range from 1.0 to 4.0 GHz. The phenomena were predicted by the classical theory of dielectrics^{36,37} due to the change in the contribution of various dielectric polarization mechanisms. The loss factor of permittivity was derived from the irradiation-time dependent derivative response component of the same materials. All the measured values of ϵ''_r in the three samples exhibited different patterns in the frequency range of 0.5–4.5 GHz.

In the case of 2 NPs, the measured loss factor values were found to be independent of the frequency. It is also noteworthy pointing out that almost all the ϵ''_r values decrease with the increase of frequency. Compared with all samples studied, the 2 NPs showed a much higher increase in the value of the imaginary part (loss factor) of the complex electric permittivity comparable to those of the real part (dielectric constant).

The tunability study of reflective SAR signal images were performed by the measurement of a triangular glass plate with/without the coating of 2 in a thin film under LED-white light illumination for a period of 5.0 and 30 min. Both electrical and magnetic properties were accounted in the measurement. The signal scanning is conducted in both vertical and horizontal directions to obtain the scattering image (or signal image) of the target. Information contained in SAR images (*e.g.*, shape, amplitude) can be used for assessing the scattering response of an object, which is dependent on the dielectric properties of the object. From the signal images scanned in different directions, we determined the geometry of the triangular glass plate first. The same plate was subsequently partially coated with 2 using PDMS as the matrix material to form a thin film in a defined area and, subsequently, illuminated for a predefined period.

All scanned images were transformed by stripmap SAR image reconstruction. They were first convoluted by a target amplitude function in a Fourier transform, followed by projection to the synthetic aperture or slow-time domain. The Fresnel approximation was then used to deconvolute these signals in the synthetic aperture domain. A two-dimensionally matched filtering of the measured signals was performed with a reference signal that is calculated by a fast-time matched filter in the frequency domain. The filtered signals in the frequency domain were then multiplied by a phase function to become the target function of the measured signals. It was followed by performing an inverse Fourier transform to project the target function from the frequency domain back to the space domain, resulting in stripmap SAR images. The final back-projected SAR image amplitude $I(r, r_x)$ in the range–cross-range plane is represented by:

$$I(r, r_x) = \int_{-\infty}^{\infty} h\left(t - \frac{2r'}{c}\right) \exp\left(-4i\pi\frac{r'}{\lambda}\right) A(r') \int_0^{R_x} S(r', r'_x) a\left(\frac{r_x - r'_x}{R_0}\right) \exp(iF(r_x - r'_x)^2) dr'_x dr' \quad (1)$$

where r is the range, r_x is the cross-range, h is a matched filter, t is the time, c is the speed of light, λ is the wavelength, A is a function accounting for the antenna pattern, processing gain and the range spreading loss, S is the scattering amplitude, a is the two-way amplitude azimuth antenna pattern, R_0 is the range location of the radar, and F is a focusing function. Details of the formula can be found elsewhere.³⁸

Three SAR images are displayed in Fig. 7. They were collected by using the experimental setup given in Fig. 8 and elucidated by the stripmap SAR image reconstruction equation

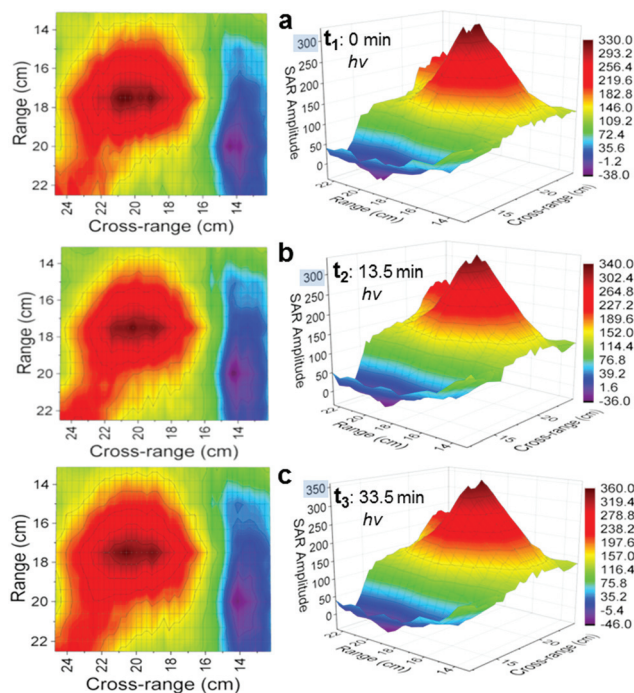


Fig. 7 Distant monostatic reflective SAR images of a triangular glass plate partially coated with 2. (a) Image profile with no light. (b) After 15 min. (c) After 30 min of LED-white light illumination. It shows signal amplification going from t_1 to t_3 at 0.5–4.0 GHz.

shown above. The total reflectivity measured in each experiment was counted to indicate the overall response of the target to the signal profile changes. We used the collected responses at t_1 (Fig. 7a, without irradiation) as the reference baseline for comparison. Various reflectivity amplitude peak profiles and photoinduced intensity changes over the range (vertical direction) and cross-range (horizontal direction) of measurements were evaluated for the signal comparison. As a result, total reflectivity changes from 113 768 (Fig. 7a) to 116 117 units (Fig. 7b) were detected after illumination for 13.5 min. The image was accompanied by a certain degree of 3D amplitude shifts in the profile. Due to the fact that the ratio of the applied coating zone to the full plate area is only $\sim 7.0\%$, the overall signal amplitude value changes revealed an effective 29.54% increase of reflectivity. This can be correlated to the same amount of response efficiency produced by the coated area of the photoexcited $C_{60}(>DPAF-C_9)$ -encapsulated $\gamma\text{-FeO}_x@AuNPs$ in the PDMS thin film. Similar measurement using a longer illumination period of 30 min led to the total reflectivity amplitude changes further to 121 651 units. This value increase corresponds to effective reflectivity amplification by a factor of $\sim 99\%$. All observations are found to be consistent with our dielectric measurements in the frequency range of 0.5–4.0 GHz, giving a demonstration of feasibility in terms of tunability and modulation ability of SAR-signals by 2 by either increase or decrease of its reflectivity to alter the image effectively.

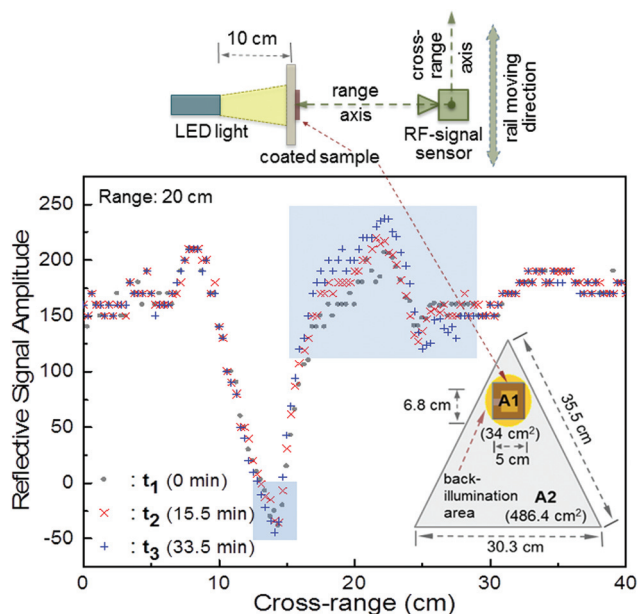


Fig. 8 Cross-range reflective signal amplitude of a 2-coated triangular glass plate (inset, core-shell sample-coated A1 area with uncoated A2 area) with or without LED-white back-light illumination; t_1 , no light; t_2 , 15 min; t_3 , 30 min irradiation. Experimental setup configuration is shown on the top.

By a particular single-point comparison using a 2D plot for easy visualization of reflective signal amplitude changes, we provided an example at a specific vertical range distance of 20 cm to display the SAR-signal amplitude profile *vs.* the horizontal cross-range distance obtained under three different light conditions, as shown in Fig. 8. A clear deviation of reflective signals in amplitude was observed at the cross-range of 15–27 cm as marked by a grey-shaded square and slight changes at 13–15 cm. Progressive increase of changes was found to be light fluence-dependent with higher values of change by a 30 min irradiation (t_3) than those with 15 min irradiation (t_2) or without illumination (t_1).

Conclusions

We fabricated highly magnetic $\gamma\text{-FeO}_x\text{@AuNP}$ core-shell nanoparticles with the deposition of a fullerosome array of $\text{C}_{60}(>\text{DPAF-C}_9)$ molecules at the outer shell. These surface-stabilized soluble NPs were found to be capable of photoinducing the SPR effect in the inner Au layer by white LED light and subsequently transfer the accumulated SPR energy at the interface to the outer, partially bilayered 1-derived fullerosome membrane layer in a near-field (~ 1.5 nm) in a configuration of a three-layered core-shell $(\gamma\text{-FeO}_x\text{@AuNP})\text{@[C}_{60}(>\text{DPAF-C}_9)]_n$. The effect led to the observation of unexpectedly large amplification of the dielectric properties associated with the photo-switching effect and the new unusual phenomenon of delayed photoinduced capacitor-like (*i.e.* electric polarization) behavior

at the frequency range of 0.5–4.0 GHz. The origin of the latter event requires further investigation. We propose the plasmonic energy activation of electron-polarization in the fullerosomic construct, consisting of covalently bound e^- -accepting C_{60} cages and e^- -donating DPAF- C_9 organic chromophores, to be the main mechanism contributing to the detected photo-switchable dielectric constant (ϵ'_r) amplification. The occurrence was followed by the relaxation of both ϵ'_r and ϵ''_r back to their initial values that revealed an excellent recyclability. Interestingly, no obvious plasmonic energy-derived thermal heat was measured by monitoring the temperature during the full experimental cycle. Based on the result, it was revealed that the formation of the intramolecular charge-separated transient state of $\text{C}_{60}^{\cdot-}(>\text{DPAF}^+\text{-C}_9)$ from **1** in **2** can also be induced by the released SPR energy in this experiment in addition to the previously known similar effect by photoexcitation of the DPAF- C_9 moiety *via* visible light. Furthermore, we suggest that the fullerosome array of C_{60} cages in the membrane provides the pathway for long-lived charge-delocalized $(\text{C}_{60}^{\cdot-})^n$ ($n \geq 1$) among nanocages, leading partly to large dielectric constant increases. The effect may be suitable for creating photoresponsive dielectric-switchable nanomaterials toward applications of GHz frequency devices. The influence of magnetism contributed from $\gamma\text{-FeO}_x$ NPs to the measured permittivity and the profile of SAR images could be a complex matter that requires further investigation.

Acknowledgements

The authors at UML acknowledge financial support of The Air Force Office of Scientific Research (AFOSR) under the grant numbers FA9550-09-1-0380 and FA9550-14-1-0153.

References

- 1 For a recent review: D. R. Smith, J. B. Pendry and M. C. K. Wiltshire, *Science*, 2004, **305**, 788–792.
- 2 V. G. Veselago, *Sov. Phys. Usp.*, 1968, **10**, 509–514.
- 3 J. B. Pendry, D. Schurig and D. R. Smith, *Science*, 2006, **312**, 1780–1782.
- 4 J. A. Kong, B.-I. Wu and Y. Zhang, *Microw. Opt. Technol. Lett.*, 2002, **33**, 136–139.
- 5 T. Kimura, T. Goto, H. Shintani, K. Ishizaka, T. Arima and Y. Tokura, *Nature*, 2003, **426**, 55–58.
- 6 A. Kumar, G. L. Sharma, R. S. R. Katiyar, R. Pirc, R. Blinc and J. F. Scott, *J. Phys.: Condens. Matter.*, 2009, **21**, 382204–382211.
- 7 L. Yan, M. Wang, R. Nandyala, A. Epstein, L.-S. Tan, A. Urbas, L. Y. Chiang and B. Hu, *J. Am. Chem. Soc.*, 2012, **134**, 3549–3554.
- 8 D. A. Bonnell, *Science*, 2013, **339**, 401–402.
- 9 S. Horiuchi, F. Ishii, R. Kumai, Y. Okimoto, H. Tachibana, N. Nagaosa and Y. Tokura, *Nat. Mater.*, 2005, **4**, 163–166.

- 10 S. Horiuchi, R. Kumai and Y. Tokura, *Angew. Chem., Int. Ed.*, 2007, **46**, 3497–3501.
- 11 S. Horiuchi and Y. Tokura, *Nat. Mater.*, 2008, **7**, 357–366.
- 12 F. Kagawa, S. Horiuchi, M. Tokunaga, J. Fujioka and Y. Tokura, *Nat. Phys.*, 2010, **6**, 169–172.
- 13 J. Wang, J. B. Neaton, H. Zheng, V. Nagarajan, S. B. Ogale, B. Liu, D. Viehland, V. Vaithyanathan, D. G. Schlom, U. V. Waghmare, N. A. Spaldin, K. M. Rabe, M. Wuttig and R. Ramesh, *Science*, 2003, **299**, 1719–1722.
- 14 Y. Xu, *Ferroelectric Materials and Their Applications*, Elsevier Science Publishers, 1991, ISBN 0-444-88354-1.
- 15 M. Lines and A. Glass, *Principles and Applications of Ferroelectrics and Related Materials*, Clarendon Press, Oxford, 1979, ISBN 0-19-851286-4.
- 16 Y. Wang, J. Hu, Y. Lin and C.-W. Nan, *NPG Asia Mater.*, 2010, **2**, 61–68.
- 17 Y. M. Sheu, S. A. Trugman, L. Yan, C.-P. Chun, Z. Bi, Q. X. Jia, A. J. Taylor and R. P. Prasankumar, *Cond. Mat. Mtrl. Sci.*, 2012, arXiv:1212.3046v1.
- 18 J.-S. Hong and Y.-H. Chun, *PIERS Online*, 2008, **4**, 726–730.
- 19 A. S. Tatarenko, M. I. Bichurin and G. Srinivasan, *Electron. Lett.*, 2005, **41**, 596–597.
- 20 C. V. Weiss, M. B. Okatan, S. P. Alpay, M. W. Cole, E. Ngo and R. C. Toonen, *J. Mater. Sci.*, 2009, **44**, 5364–5374.
- 21 M. B. Shelar, R. N. Jadhav and V. Puri, *Prog. Electromagn. Res.*, 2010, **17**, 55–65.
- 22 D. P. Makhnovskiy and L. V. Panina, *J. Appl. Phys.*, 2003, **93**, 4120–4129.
- 23 P. A. Padmawar, T. Canteenwala, S. Verma, L.-S. Tan, G. S. He, P. N. Prasad and L. Y. Chiang, *Synth. Met.*, 2005, **154**, 185–188.
- 24 P. A. Padmawar, T. Canteenwala, L.-S. Tan and L. Y. Chiang, *J. Mater. Chem.*, 2006, **16**, 1366–1378.
- 25 P. A. Padmawar, J. O. Rogers, G. S. He, L. Y. Chiang, T. Canteenwala, L.-S. Tan, Q. Zheng, C. Lu, J. E. Slagle, E. Danilov, D. G. McLean, P. A. Fleitz and P. N. Prasad, *Chem. Mater.*, 2006, **18**, 4065–4074.
- 26 D. M. Guldi and M. Prato, *Acc. Chem. Res.*, 2000, **33**, 695–703.
- 27 D. M. Guldi and P. V. Kamat, *Fullerenes, Chemistry, Physics and Technology*, ed. K. M. Kadish and R. S. Ruoff, Wiley-Interscience, New York, 2000, pp. 225–281.
- 28 M. Maggini and D. M. Guldi, *Molecular and Supramolecular Photochemistry*, ed. V. Ramamurthy and K. S. Schanze, Marcel Dekker, New York, 2000, vol. 4, pp. 149–196.
- 29 M. Wang, S. Jeon, C. Su, T. Yu, L.-S. Tan and L. Y. Chiang, *Molecules*, 2015, **20**, 14746–14760.
- 30 J. Park, K. An, Y. Hwang, J.-G. Park, H.-J. Noh, J.-Y. Kim, J.-H. Park, N.-M. Hwang and T. Hyeon, *Nat. Mater.*, 2004, **3**, 891–895.
- 31 M. E. El-Khouly, R. Anandakathir, O. Ito and L. Y. Chiang, *J. Phys. Chem. A*, 2007, **111**, 6938–6944.
- 32 H. I. Elim, R. Anandakathir, R. Jakubiak, L. Y. Chiang, W. Ji and L. S. Tan, *J. Mater. Chem.*, 2007, **17**, 1826–1838.
- 33 S. Verma, T. Hauck, M. E. El-Khouly, P. A. Padmawar, T. Canteenwala, K. Pritzker, O. Ito and L. Y. Chiang, *Langmuir*, 2005, **21**, 3267–3272.
- 34 V. Yong and H. T. Hahn, *Adv. Nanopart.*, 2013, **2**, 1–5.
- 35 H. Luo, M. Fujitsuka, Y. Araki, O. Ito, P. Padmawar and L. Y. Chiang, *J. Phys. Chem. B*, 2003, **107**, 9312–9318.
- 36 P. Debye, *Polar Molecules*, The Chemical Catalog Company, New York, NY, 1929.
- 37 C. P. Smyth, *Dielectric Behavior and Structure*, McGraw-Hill, New York, NY, 1955.
- 38 M. Soumekh, *Synthetic Aperture Radar Signal Processing with MATLAB Algorithms*, Wiley, New York, NY, 1999.